nuclear fusion
IAEA

PAPER

A multi-machine scaling of halo current rotation

To cite this article: C.E. Myers *et al* 2018 *Nucl. Fusion* **58** 016050

View the article online for updates and enhancements.

Related content

- The ITPA disruption database
N.W. Eidietis, S.P. Gerhardt, R.S. Granetz et al.
- The halo current in ASDEX Upgrade
G. Pautasso, L. Giannone, O. Gruber et al.
- Characterization of disruption halo currents in the National Spherical Torus Experiment
S.P. Gerhardt, J. Menard, S. Sabbagh et al.

Recent citations

- KSTAR Status and Upgrade Plan Toward Fusion Reactor
Jong-Gu Kwak *et al*
- Dependence of disruption forces on the plasma position inside the vacuum vessel in tokamaks
V D Pustovitov
- Overview of disruptions with JET-ILW
S.N. Gerasimov *et al*

IOP ebooks™

Bringing together innovative digital publishing with leading authors from the global scientific community.

Start exploring the collection–download the first chapter of every title for free.

This content was downloaded from IP address 37.158.234.192 on 20/07/2020 at 12:09

IOP Publishing | International Atomic Energy Agency Nuclear Fusion

Nucl. Fusion **58** (2018) 016050 (15pp) https://doi.org/10.1088/1741-4326/aa958b

A multi-machine scaling of halo current rotation

C.E. Myers[1], N.W. Eidietis[2], S.N. Gerasimov[3], S.P. Gerhardt[1], R.S. Granetz[4], T.C. Hender[3], G. Pautasso[5] and JET Contributors[a]

[1] Princeton Plasma Physics Laboratory, Princeton, NJ 08543, United States of America
[2] General Atomics, San Diego, CA 92186, United States of America
[3] CCFE, Culham Science Centre, Abingdon, OX14 3DB, United Kingdom
[4] MIT Plasma Science and Fusion Center, Cambridge, MA 02139, United States of America
[5] Max-Planck-Institüt für Plasmaphysik, D-85748 Garching, Germany

E-mail: cmyers@pppl.gov

Received 23 May 2017, revised 29 September 2017
Accepted for publication 24 October 2017
Published 12 December 2017

Abstract

Halo currents generated during unmitigated tokamak disruptions are known to develop rotating asymmetric features that are of great concern to ITER because they can dynamically amplify the mechanical stresses on the machine. This paper presents a multi-machine analysis of these phenomena. More specifically, data from C-Mod, NSTX, ASDEX Upgrade, DIII-D, and JET are used to develop empirical scalings of three key quantities: (1) the machine-specific minimum current quench time, τ_{CQ}; (2) the halo current rotation duration, t_{rot}; and (3) the average halo current rotation frequency, $\langle f_h \rangle$. These data reveal that the normalized rotation duration, t_{rot}/τ_{CQ}, and the average rotation velocity, $\langle v_h \rangle$, are surprisingly consistent from machine to machine. Furthermore, comparisons between carbon and metal wall machines show that metal walls have minimal impact on the behavior of rotating halo currents. Finally, upon projecting to ITER, the empirical scalings indicate that substantial halo current rotation above $\langle f_h \rangle = 20$ Hz is to be expected. More importantly, depending on the projected value of τ_{CQ} in ITER, substantial rotation could also occur in the resonant frequency range of 6–20 Hz. As such, the possibility of damaging halo current rotation during unmitigated disruptions in ITER cannot be ruled out.

Keywords: tokamak, disruptions, halo currents

(Some figures may appear in colour only in the online journal)

1. Introduction

When a tokamak plasma disrupts, large electric currents are driven in the conducting walls that surround the plasma [1–8]. A portion of these wall currents are eddy currents induced by the disrupting plasma [9], while the remainder are so-called halo currents that are driven when the plasma makes direct contact with the wall [10, 11]. Inside the wall, both eddy and halo currents can flow across magnetic field lines and produce large $\mathbf{J} \times \mathbf{B}$ Lorentz forces that can jeopardize the structural integrity of the machine [9, 12, 13]. Given the increasing size and parameters of next-generation tokamaks such as ITER, these wall-current-generated forces pose a significant threat to the viability of the tokamak as a fusion reactor concept [14–20]. As such, it is imperative to understand how the various disruption wall current phenomena will scale in next-generation devices.

In this paper, we focus on the behavior of halo currents, which flow along a hybrid current path that connects the scrape-off layer of the plasma to the wall of the machine. This plasma-wall circuit enables the direct measurement of the halo currents as they enter or exit the first wall [21, 22]. Such measurements reveal that halo currents often develop toroidal asymmetries [3–8, 23–26] that are attributed to a magneto-hydrodynamic kink mode [27–31] that destabilizes when the

[a] See the author list of 'Overview of the JET results in support to ITER' by Litaudon *et al* [52].

 © 2017 Princeton University Plasma Physics Laboratory Printed in the UK

edge safety factor drops below $q_{95} \sim 2$ [32]. The resulting helically kinked plasma only makes contact with a finite toroidal section of the wall such that the halo currents are preferentially driven in a toroidally localized region. This generates toroidally asymmetric forces that manifest themselves, for example, as strong lateral impulses in large tokamaks such as JET [9, 23, 25]. Given that toroidal halo current asymmetries are largely ameliorated by disruption mitigation systems such as massive gas injection (MGI) [33, 34], we focus in this paper on halo currents generated during unmitigated disruptions.

An additional consideration regarding asymmetric halo currents is that the location of the asymmetry often rotates toroidally during the disruption [3, 7, 35–37]. At first glance, this rotation might seem to be beneficial because it reduces the directional coherence of the lateral or vertical impulse delivered to the machine. This benefit becomes a detriment, however, if the halo currents complete 2–3 full rotations at a frequency that resonates with critical machine components. Such resonant rotation can produce dynamically amplified forces that enhance the overall structural loads. For ITER, the critical coil and vessel resonances are in the 3–8 Hz range, while integrated system resonances extend into the 10–20 Hz band [18, 19]. Thus, the rotating halo current problem in ITER can be summarized in a single question: Are halo currents in ITER likely to complete 2–3 full rotations at frequencies below 20 Hz?

The goal of this paper is to answer this question by developing an empirical scaling of halo current rotation that can be extrapolated to ITER. Though halo current rotation has been observed in a number of devices [3, 7, 35–37] and explored with theory [38, 39] and simulations [40], no experimental investigation of how it scales with machine parameters has yet been conducted. The approach used here is to assemble a multi-machine database of toroidally resolved halo current measurements and then to process these data within a common analytical framework. This undertaking, which is conducted under the auspices of the International Tokamak Physics Activity (ITPA), facilitates the development of empirical scalings for three key quantities: (1) the machine-specific minimum current quench time, τ_{CQ}; (2) the halo current rotation duration, t_{rot}; and (3) the time-averaged halo current rotation frequency, $\langle f_h \rangle$. When combined, the latter two quantities characterize the total rotation count, N_{rot}, at a given rotation frequency:

$$N_{rot} = \langle f_h \rangle \cdot t_{rot} = \frac{\langle v_h \rangle}{2\pi R} \cdot t_{rot}, \quad (1)$$

where $\langle v_h \rangle$ is the time-averaged toroidal rotation velocity and R is the major radius of the machine. In this paper, we use a newly constructed ITPA halo current rotation database to empirically determine how τ_{CQ}, t_{rot}, and $\langle f_h \rangle$ scale with key machine parameters. Once these scalings are established, a prediction can be made as to which rotation frequencies are likely to complete at least 2–3 rotations in ITER.

The remainder of the paper is organized as follows: in section 2, the format and contents of the ITPA halo current rotation database are described. Then, in section 3, a scaling of the machine-specific minimum current quench time, τ_{CQ}, is developed. This scaling ultimately facilitates the projection of the behavior of rotating halo currents to ITER. Next, in section 4, we analyze the properties of rotating halo currents, including their rotation frequency and velocity as well as their preferred direction of rotation. Then, in sections 5.1 and 5.2, we use the results of sections 3 and 4 to develop empirical scalings of the halo current rotation duration, t_{rot}, and rotation frequency, $\langle f_h \rangle$. In section 5.3, these scalings are used to project the behavior of rotating halo currents in ITER. Finally, in section 6, we close with a discussion of candidate physical mechanisms that may explain some of the halo current rotation phenomena reported here.

Table 1. Contents of the ITPA halo current rotation database. Seven total datasets, delineated by machine and wall material, are sourced from five different machines. Only unmitigated disruptions are included. In total, the database contains 813 shots, each of which terminates with an asymmetric vertical displacement event (VDE). Note that the database does not necessarily include all of the unmitigated disruptions from each machine. For example, the 150 shots in the JET-ILW dataset are the 150 most asymmetric disruptions out of ~6500 total disruptions recorded for JET-ILW.

Machine	Wall material	Sensor type	Shots
C-Mod	Molybdenum	Partial rogowskis	148
NSTX	Carbon	Shunt tiles (1 row)	141
AUG-C	Carbon	Shunt tiles (2 rows)	129
AUG-W	Tungsten	Shunt tiles (2 rows)	49
DIII-D	Carbon	Shunt tiles (5 rows)	51
JET-C	Carbon	I_p asymmetry	145
JET-ILW	ITER-like	I_p asymmetry	150
Total			813

2. The ITPA halo current rotation database

In order to develop a multi-machine scaling of halo current rotation, a new database of toroidally resolved halo current measurements is required. The approach taken here is to collect raw halo current data (e.g. shunt tile waveforms) from a number of devices that have deployed toroidally resolved halo current sensor arrays. The resulting ITPA halo current rotation database therefore contains a substantial amount of raw data that are processed within a common analytical framework.

The new ITPA halo current rotation database includes data from five tokamaks: Alcator C-Mod [3], DIII-D [35], ASDEX Upgrade (AUG) [7], NSTX [36], and JET [34, 37]. These machines collectively span a wide range of spatial scales and equilibrium parameters so that the scaling of halo current rotation with a variety of machine parameters can be assessed. The impact of the wall material (metal versus carbon), for example, is a key concern when extrapolating from present-day tokamaks to ITER, which will use a tungsten-and-beryllium metal wall. As such, data from both carbon and metal wall machines are included in the database. Table 1 lists the various datasets in the ITPA halo current rotation database, separated by machine and wall material. Four of the datasets (DIII-D, NSTX, AUG-C, and JET-C) were acquired during carbon wall operations, while the three remaining datasets (C-Mod, AUG-W, and JET-ILW) were acquired during metal

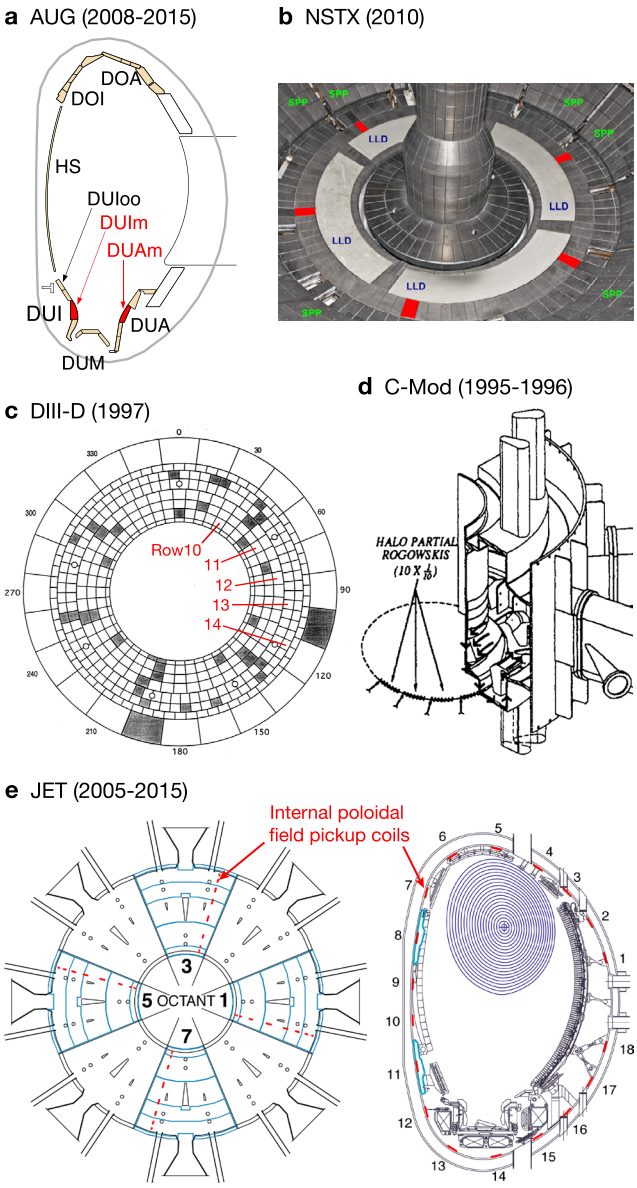

Figure 1. The toroidally resolved halo current sensor arrays in the ITPA halo current rotation database. (*a*) Two shunt tile arrays (DUIm, DUAm) in the lower divertor of ASDEX Upgrade. Reproduced courtesy of IAEA. Figure from [7]. Copyright 2011 IAEA. (*b*) A single shunt tile array in the lower outboard divertor of NSTX (red). Reproduced courtesy of IAEA. Figure from [36]. Copyright 2013 IAEA. (*c*) Five shunt tile arrays (Rows 10–14) in the lower divertor of DIII-D [21]. (*d*) A single partial rogowski array in the lower inboard divertor of C-Mod. Reproduced courtesy of IAEA. Figure from [3]. Copyright 1996 IAEA. (*e*) Four octants of poloidal field sensor arrays (red) to measure plasma current asymmetries in JET. Reproduced courtesy of IAEA. Figure from [37]. © 2014 EURATOM.

wall operations. The specific metals used in each machine (molybdenum, tungsten, or ITER-like tungsten and beryllium) are listed in table 1. The dual datasets from AUG (carbon and tungsten) and JET (carbon and ITER-like) are particularly valuable in that they provide intra-machine comparisons of how halo currents are modified by metal walls.

The machines in the ITPA halo current rotation database employ several types of halo current sensors. As shown in figure 1, the halo current sensor arrays in three of the machines, AUG, NSTX, and DIII-D, are comprised of shunt tiles, which resistively measure halo currents flowing from the plasma into the wall. The AUG shunt tile sensor set (figure 1(*a*)) is comprised of an inboard array (DUIm, 9 tiles) and an outboard array (DUAm, 8 tiles) [7]. The NSTX sensor set (figure 1(*b*)) is comprised of a single row of 6 shunt tiles on the outboard side of the divertor [8, 22, 36]. The DIII-D sensor set (figure 1(*c*)) is comprised of five concentric rings of shunt tiles with 5–10 tiles each [21, 35]. In C-Mod, on the other hand, halo currents are measured using an array of 10 partial rogowski coils (figure 1(*d*)) [3]. Each partial rogowski coil measures the poloidal current in a toroidally localized region of the inner vessel wall. Two toroidally continuous rogowski coils (not shown) measure the total poloidal wall current in the upper and lower divertors. These measurements confirm that the poloidal wall currents measured in the lower divertor during a downward-moving disruption are dominated by halo currents rather than by eddy currents [3].

JET uses a third technique for measuring halo currents: the identification of toroidal asymmetries in the plasma current. Here, poloidally distributed arrays of poloidal magnetic field sensors (figure 1(*e*)) act as toroidally localized plasma current rogowski coils. Four of these sensor arrays are deployed in various 'octants' of the JET vessel such that toroidal asymmetries in the plasma current, I_p, can be identified [37]. These I_p asymmetry measurements quantify the net toroidal current difference between octants due to halo currents. While there is intense debate about the physical mechanism(s) that generate the I_p asymmetries [9, 28, 37], the JET I_p asymmetry measurements can be used in the same way as poloidally localized measurements in other machines to characterize halo current phenomena [41].

Finally, each entry in the ITPA halo current rotation database includes a set of auxiliary waveforms that are associated with each disruption. These waveforms include quantities such as the plasma current, I_p, the toroidal magnetic field, B_T, and various equilibrium parameters such as the major radius, R, the minor radius, a, the elongation, κ, the edge safety factor, q_{95}, the internal inductance, ℓ_i, and the stored energy, W_{MHD}. In some cases, additional data is available concerning the evolution of the plasma's vertical position, Z_p, and cross-sectional area, S. In this paper, however, the analysis of auxiliary waveforms is limited primarily to I_p and B_T.

In total, the ITPA halo current rotation database includes more than 800 discharges (shots) spread across seven datasets from five different machines. Table 1 summarizes the machine, wall material, sensor type, and shot count for each of the seven datasets. Importantly, since disruption mitigation schemes such as massive gas injection (MGI) are known to suppress halo current asymmetries [33, 34], only unmitigated disruptions are considered in this study. To ensure that this is the case, information on the triggering of various disruption mitigation systems is also included in the database. This information, along with an analysis of the asymmetry of the halo currents (section 4), is used to filter the database to include only unmitigated disruptions that terminate in an asymmetric vertical displacement event (VDE). All 813 shots listed in table 1 satisfy these criteria.

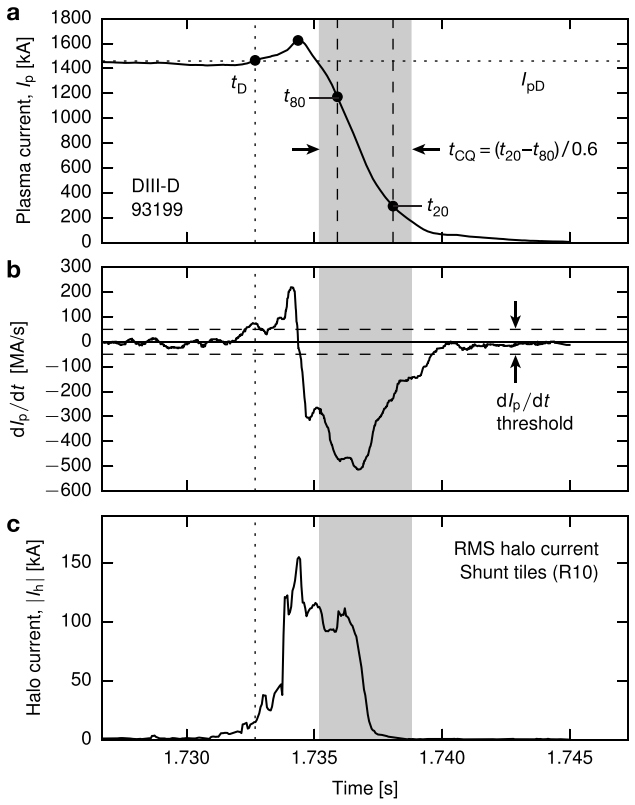

Figure 2. The disruption current quench analysis procedure. (*a*) The plasma current waveform, $I_p(t)$, is processed to identify the disruption time, t_D, the pre-disruption plasma current, I_{pD}, and the 80% and 20% times, t_{80} and t_{20}. The discharge-specific current quench time is defined as $t_{CQ} \equiv (t_{20} - t_{80})/0.6$ [14] and is shaded in gray. (*b*) A threshold of $|dI_p/dt| = 50$ MA s^{-1} is used to identify the current spike (if there is one) and to identify the disruption time, t_D. (*c*) The RMS halo current waveform, $|I_h(t)|$, for the Row 10 shunt tiles as determined from equation (2) shows that the halo current rises sharply at the time of the current spike and persists well into the current quench.

3. Disruption current quench analysis

Each disruption in the ITPA halo current rotation database is first analyzed for its current quench properties. In this section, we analyze these current quench properties in detail because, as will be shown in section 5, the scaling of halo current rotation is intimately linked to the scaling of the current quench. We begin by establishing the procedure for determining the discharge-specific current quench time, t_{CQ}. Figure 2 shows the current quench analysis for a typical DIII-D discharge. In figure 2(*a*), a disruption timing algorithm is applied to the plasma current waveform, $I_p(t)$, to determine the disruption time, t_D, the pre-disruption plasma current, $I_{pD} \equiv I_p(t_D)$, and the 80% and 20% times, t_{80} and t_{20}. The algorithm searches for a current spike and determines the disruption time based on a threshold applied to dI_p/dt (see figure 2(*b*)). Here, a threshold value of $|dI_p/dt| = 50$ MA s^{-1} is used in all cases. For JET discharges specifically, the disruption time, t_D, is determined using the algorithm of Gerasimov *et al*, which monitors the loop voltage in addition to dI_p/dt [34, 37]. In either case, the resulting discharge-specific current quench time is defined as $t_{CQ} \equiv (t_{20} - t_{80})/0.6$ [14].

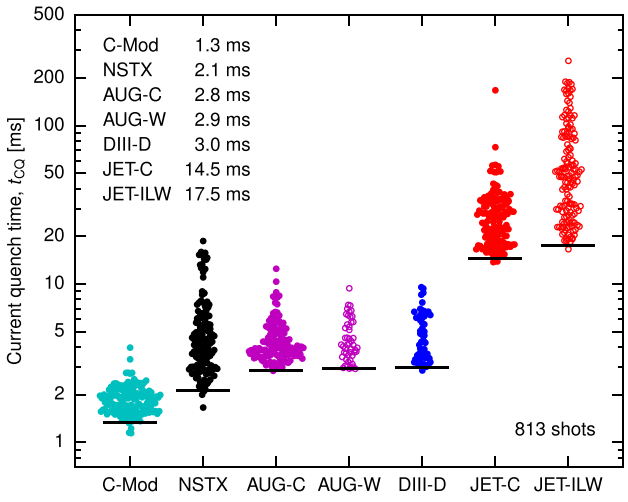

Figure 3. Measured current quench times, t_{CQ}, across the ITPA halo current rotation database, sorted by machine. The horizontal width of each dataset is a histogram of the distribution of current quench times in that dataset. Though a wide range of quench times are observed, each machine is subject to a sharp lower limit on how quickly the plasma current can quench during a disruption. The empirical values for this minimum current quench time, τ_{CQ}, are defined as the lower bound of the first histogram bin that contains 20% as many points as the fullest histogram bin. The resulting τ_{CQ} values are plotted as horizontal black lines and listed in the legend. The histogram bins are distributed logarithmically such that the error in each τ_{CQ} value is ±5%. Note that the τ_{CQ} values for AUG-W versus AUG-C and JET-ILW versus JET-C are comparable, indicating that τ_{CQ} is largely unaffected by the wall material in this database of asymmetric VDEs.

To highlight the timing of the halo currents with respect to the current quench, figure 2(*c*) shows the RMS halo current waveform, $|I_h(t)|$, from one of DIII-D's toroidally resolved shunt tile arrays (Row 10, see figure 1). Here, the $|I_h(t)|$ waveform is defined as

$$|I_h(t)| = \sqrt{\sum_i^{N_{sens}} \frac{\Delta\phi_i}{\delta\phi_i} [I_h(t,\phi_i)]^2}, \quad (2)$$

where N_{sens} is the number of sensors in the array, ϕ_i is the toroidal location of the ith sensor, $\delta\phi_i$ is the toroidal extent of the ith sensor, $\Delta\phi_i$ is the toroidal extent of the vessel sector represented by the ith sensor, and $I_h(t,\phi_i)$ is the halo current measured by the ith sensor. The resulting $|I_h(t)|$ waveform represents the toroidally integrated halo current flowing into or out of a poloidally localized region of the divertor. The sample $|I_h(t)|$ waveform in figure 2(*c*) rises with the plasma current spike at the start of the disruption and persists well into the current quench. We note here that, in most cases, the halo current measured by a given sensor array is only a fraction of the total halo current since most of the arrays are poloidally localized.

The current quench analysis procedure described in figure 2 is applied to all disruptions in the ITPA halo current rotation database. Figure 3 shows the resulting database-wide variation of the shot-specific current quench time, t_{CQ}. Here, the x-axis separates the data by machine, while the y-axis plots the measured values of t_{CQ}. The horizontal width of each dataset

is a histogram of the distribution of current quench times. Figure 3 shows that each machine exhibits a wide range of t_{CQ} values that can vary by up to an order of magnitude within a given machine. A clear feature of these data is that each device is subject to a sharp lower limit on t_{CQ}. We define this lower limit as the characteristic minimum quench time, τ_{CQ}. The τ_{CQ} value for each machine is determined here as the lower bound of the first histogram bin that contains 20% as many points as the fullest histogram bin (in order to avoid outliers). The resulting τ_{CQ} values, which are plotted as horizontal black lines in figure 3, vary from 1.3 ms for C-Mod to 17.5 ms for JET-ILW. The histogram bins are distributed logarithmically such that the error in each τ_{CQ} value is $\pm 5\%$. One key result is that the τ_{CQ} values for AUG-W and JET-ILW are not meaningfully different from their carbon-wall counterparts (AUG-C and JET-C, respectively). This implies that, while metal wall machines are capable of producing very long current quenches [33, 42], the minimum current quench time, τ_{CQ}, is largely unaffected by the wall material. These results are consistent with previous JET analyses, which show (1) that unmitigated 'fast VDEs' quench on equally rapid timescales in both JET-C and JET-ILW [33, 42]; and (2) that these fast VDEs are often asymmetric in nature [34]. Given the apparent insensitivity of τ_{CQ} to the wall material, the AUG and JET datasets will be combined for the remainder of this section.

In order to project the observed current quench behavior to ITER, it is necessary to develop a scaling for the minimum current quench time, τ_{CQ}. Previously, Wesley *et al* used the ITPA Disruption Database to empirically connect τ_{CQ} to the $\mathcal{L}/\mathcal{R}$ inductive decay time of the plasma [14, 17]. Reestablishing this connection for the present ITPA halo current rotation database is key because the $\mathcal{L}/\mathcal{R}$ inductive decay time can be readily computed from the geometric parameters of each machine.

The inductive decay time of the plasma is defined as $\tau_{ind} = \mathcal{L}/\mathcal{R}$, where $\mathcal{L}$ is the plasma inductance and $\mathcal{R}$ is the plasma resistance. The plasma inductance is well-described by that of a toroidal current ring:

$$\mathcal{L} = \mu_0 R\,\ell = \mu_0 R\left[\ln\left(\frac{8R}{a}\right) - 2 + \frac{\ell_i}{2}\right], \qquad (3)$$

where R is the plasma major radius, ℓ is the normalized inductance, a is the plasma minor radius, and ℓ_i is its internal inductance. The plasma resistance, $\mathcal{R}$, on the other hand, is given by

$$\mathcal{R} = \eta\left(\frac{2\pi R}{S}\right), \qquad (4)$$

where η is the plasma resistivity and S is its cross-sectional area. Combining equations (3) and (4), the plasma's inductive decay time is given by

$$\tau_{ind} = \mathcal{L}/\mathcal{R} = \frac{\mu_0}{2\pi\eta} S\,\ell = C\left(\eta^{-1}\right) S\,\ell, \qquad (5)$$

where $C(\eta^{-1})$ is a prefactor that depends primarily on the characteristic resistivity of the disrupting plasma.

Following Wesley *et al*, we now demonstrate the connection between the minimum current quench time, τ_{CQ}, and the inductive decay time, τ_{ind} [14]. Figure 4 plots the database-wide

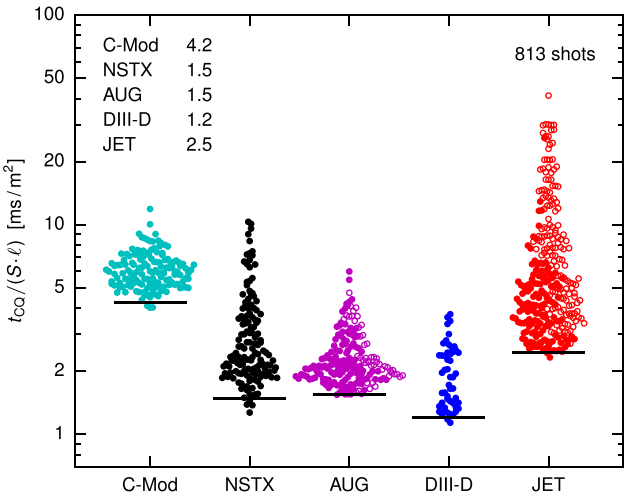

Figure 4. Current quench times, t_{CQ}, normalized to the product of the plasma cross-sectional area, S, and the normalized inductance, ℓ (equation (5)). The AUG and JET databases are combined as per the discussion in the text. The black horizontal lines represent the normalized minimum quench times, $C(\eta^{-1}) \equiv \tau_{CQ}/(S\cdot\ell)$, which are listed in the legend. These results, which are quantitatively consistent with the ITPA Disruption Database [14, 17, 43], identify $C(\eta^{-1}) = 1.2$–4.2 ms m^{-2} as the range to be used when projecting τ_{CQ} to ITER.

current quench times, t_{CQ}, normalized to the product of the plasma cross-sectional area, S, and the normalized inductance, ℓ. The S, R, and a values used in the computation of the $S\cdot\ell$ product are extracted from a pre-disruption equilibrium reconstruction of each discharge. In keeping with Wesley *et al* [14], a flat post-thermal-quench current profile is assumed ($\ell_i = 0.5$). The data in figure 4, which are quantitatively consistent with the ITPA Disruption Database [14, 17, 43], identify $C(\eta^{-1}) = 1.2$–4.2 ms m^{-2} as the range to be used when projecting τ_{CQ} to ITER. The machines that define the extrema in this range, C-Mod (4.2 ms m^{-2}) and DIII-D (1.2 ms m^{-2}), warrant further discussion.

As derived in equations (3)–(5), the τ_{ind} prefactor, $C(\eta^{-1})$, is expected to be a function of the characteristic resistivity of the disrupting plasma, η. This resistivity is set by the core temperature in the post-thermal-quench plasma, which, in turn, is governed by the balance of two competing processes: ohmic reheating and radiative dissipation. Ohmic reheating injects energy into the post-thermal-quench plasma at a rate of ηJ^2, where J is the toroidal plasma current density. Radiative dissipation, on the other hand, sheds energy from the plasma at a rate that depends on the impurity content. In practice, the impurity content is largely determined by the wall material in the machine. Given the previous conclusion that the wall material has little impact on τ_{CQ} in this database of asymmetric VDEs, we focus here on the effect of ohmic reheating.

In the C-Mod case, it is clear that increased ohmic reheating plays a substantial role in the current quench normalization. C-Mod is a high-B_T machine that operates at current densities ($J \sim 2$–4 MA m^{-2}) that are much higher than those of other tokamaks ($J \sim 0.2$–0.6 MA m^{-2}). The high current densities in C-Mod lead to observable reheating during the disruption [3], which is likely the cause of the elevated

Table 2. Summary of the current quench timing analysis of the ITPA halo current rotation database. The $S \cdot \ell$ values for each machine in the database are computed as $S \cdot \ell = \tau_{CQ}/C(\eta^{-1})$. For ITER, on the other hand, $S \cdot \ell$ is computed using the following nominal values: $R = 6.2$ m, $a = 2$ m, and $\kappa = 1.7$. The ITER τ_{CQ} values are calculated using the projected $C(\eta^{-1})$ range of 1.2 –4.2 ms m^{-2} determined from figure 4.

Machine	$S \cdot \ell$ (m^2)	τ_{CQ} (ms)	$C(\eta^{-1})$ (ms m^{-2})
C-Mod	0.32	1.3	4.2
NSTX	1.4	2.1	1.5
AUG	1.8	2.8	1.5
DIII-D	2.5	3.0	1.2
JET	5.9	15	2.5
ITER (min)	31	37	1.2
ITER (max)	31	130	4.2

$C(\eta^{-1})$ value of 4.2 ms m^{-2}. For DIII-D, on the other hand, Wesley *et al* explored the role of a reduced external inductance as a possible explanation for the depressed $C(\eta^{-1})$ value of 1.2 ms m^{-2} [17]. Regardless of the underlying causes of the variation in the values of $C(\eta^{-1})$ in figure 4, we adopt the observed range of $C(\eta^{-1}) = 1.2$–4.2 ms m^{-2} for projecting τ_{CQ} to ITER. A summary of the database-wide current quench results obtained in this section is given in table 2. The extrapolated τ_{CQ} values for ITER are $\tau_{CQ} \simeq 37$–130 ms.

One important timescale that does not enter into the Wesley scaling is the VDE growth time, τ_{vert}. This timescale is a machine-specific parameter that is set by the electrical conductivity of the passive structures that surround the plasma. Since τ_{vert} determines how fast the plasma can drift into the wall, it, too, is expected to play a role in setting the minimum current quench time, τ_{CQ}. This is especially true in events such as unmitigated 'fast VDEs' in JET where the core remains relatively hot (and therefore non-dissipative) throughout the current quench [33]. Instead of the $\mathcal{L}/\mathcal{R}$ decay of the core plasma, the primary current quench mechanism in these cases is believed to be ohmic dissipation in the halo region as the plasma collides with the wall [44]. By happenstance, the VDE growth time in all five machines in the ITPA halo current rotation database is on the order of a few milliseconds. This τ_{vert} degeneracy prevents the development of a τ_{CQ} scaling that includes τ_{vert}, which is unfortunate given that ITER will have a much longer VDE growth time of $\tau_{vert} \sim 0.5$ s. The implications for ITER if the long VDE growth time increases τ_{CQ} beyond the values predicted by the Wesley scaling are discussed at the end of section 5.3.

4. Halo current rotation analysis

This section describes the halo current rotation analysis procedure developed for this multi-machine study. This procedure extracts the rotation duration, t_{rot}, and the rotation count, N_{rot}, from each set of toroidally resolved halo current measurements in the ITPA halo current rotation database. In conjunction with equation (1), these two quantities facilitate the development of empirical scalings of t_{rot} and the halo current rotation frequency, $\langle f_h \rangle$.

The primary objective of the halo current rotation analysis is to track the toroidal rotation of the halo current asymmetry in time. In order to do so, the raw halo current data are fitted at each time point with an $n = 1$ model function of the form

$$I_h(\phi) = h_0 + h_1 \sin(\phi - h_2), \tag{6}$$

where ϕ is the toroidal angle, h_0 is the $n = 0$ amplitude, h_1 is the $n = 1$ amplitude, and h_2 is the $n = 1$ phase. In all cases, the toroidal angle, ϕ, is defined with respect to right-handed coordinates (ϕ increases counter-clockwise from above). Signed quantities such as I_p, B_T, and N_{rot} are referenced to these right-handed coordinates. While equation (6) does not capture the full toroidal structure of the halo currents, it does provide a robust measurement of the toroidal phase of the halo current asymmetry. Sample results from this fitting procedure are presented in figure 5, which considers the halo currents during a typical NSTX disruption. In figure 5(*a*), the raw halo current data, $I_h(t, \phi)$, are plotted in color. Here, the color scale is set so that the darkest red corresponds to the maximum halo current measured during this discharge. The black line that tracks the rotation is the fitted $n = 1$ phase parameter, h_2. In this sample discharge, an asymmetric lobe of halo current initially rotates in the negative toroidal direction (clockwise from above). It then locks at a fixed toroidal location ($\phi \sim 300°$) for some time before resuming its clockwise rotation at the end of the disruption. Erratic halo current rotation patterns such as this are not uncommon; therefore, the halo current rotation analysis procedure must be robust to abrupt rotation locking or reversal.

The next step after fitting the halo current measurements with equation (6) is to identify the 'asymmetry intervals' over which the halo current asymmetry has sufficient amplitude to warrant tracking the rotation. This is accomplished here by applying a threshold to the fitted $n = 1$ amplitude, h_1 (see figure 5(*b*)). In practice, an h_1 threshold of 10 kA works well for all of the halo current sensor arrays in the database. In the sample disruption in figure 5, a single asymmetry interval is identified (the interval between the two vertical dashed lines in figures 5(*a*) and (*b*)). Note that a minimum dwell time of $\tau_{min} = 0.3\,\tau_{CQ}$ is enforced during the identification of the asymmetry interval in order to ignore brief excursions across the $h_1 = 10$ kA threshold.

Once the asymmetry interval(s) are identified, the next step is to identify 'rotation intervals' within each asymmetry interval where the halo current asymmetry is coherently rotating. At this juncture, we compute the rotation velocity waveform as $v_h(t) = R \cdot \mathrm{d}h_2/\mathrm{d}t$. After low-pass filtering $v_h(t)$ with a time constant of $\tau_{filt} = \tau_{min}/2$, the rotation intervals are identified by applying a minimum velocity threshold of $|v_h| < 0.5$ km s^{-1} (see figure 5(*c*)). Once again, a minimum dwell time of $\tau_{min} = 0.3\,\tau_{CQ}$ is enforced to ignore brief excursions across the velocity threshold. In the sample disruption in figure 5, two distinct rotation intervals are identified (the two shaded regions in figure 5(*c*)). In cases such as this where more than one rotation interval is identified, we select the

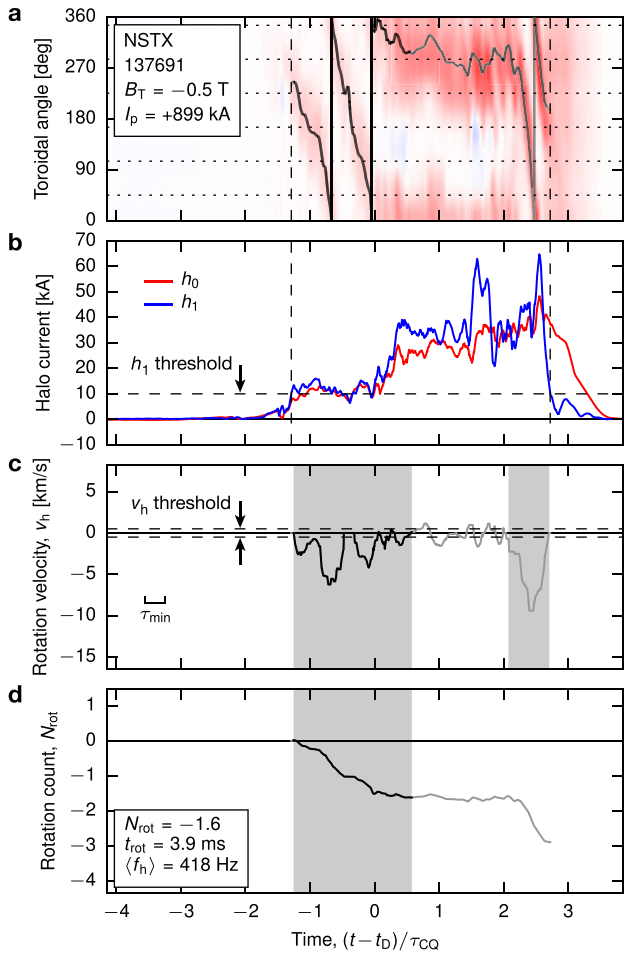

Figure 5. Sample halo current rotation analysis. The timebase is referenced to the disruption time, t_D, and normalized to the minimum current quench time, τ_{CQ}. (*a*) The raw halo current data, $I_h(t, \phi)$, is shown in color. Here, the toroidal angle, ϕ, is defined with respect to right-handed coordinates (ϕ increases counter-clockwise from above). The sensor locations are marked with horizontal dotted lines, and the black line that tracks the rotation is the fitted $n = 1$ phase parameter, h_2. (*b*) The fitted amplitude parameters, h_0 and h_1. The vertical dashed lines mark the asymmetry interval determined by applying an h_1 threshold of 10 kA and a minimum dwell time of $\tau_{min} = 0.3\,\tau_{CQ}$. (*c*) The low-pass filtered rotation velocity waveform, $v_h(t)$. Two rotation intervals (gray) are identified by applying a minimum velocity threshold of $|v_h| < 0.5$ km s^{-1} and the same minimum dwell time. (*d*) The cumulative rotation count, $N_{rot}(t)$. The scalar rotation parameters (N_{rot}, t_{rot}, $\langle f_h \rangle$) are extracted from the longer of the two rotation intervals, which is shaded in gray.

interval with the longest duration as the main rotation interval. Figure 5(*d*) shows the cumulative rotation count, $N_{rot}(t)$. The scalar rotation parameters reported for this discharge (N_{rot}, t_{rot}, $\langle f_h \rangle$) are extracted from the main rotation interval, which is shaded in gray.

With the halo current rotation analysis procedure in hand, we now investigate sample halo current measurements from each machine. In the examples shown in figure 6, the color of the various halo current measurements represents their polarity. More specifically, a positive halo current (red) is defined as halo current leaving the wall and entering the plasma, while a negative halo current (blue) is defined as halo current leaving the plasma and entering the wall. In the C-Mod, NSTX, AUG, and DIII-D examples, the halo currents possess a prevailing polarity that is associated with the poloidal localization of the halo current sensors. In the JET examples, on the other hand, the I_p asymmetry measurements are symmetric about zero such that no polarity information is available. It is interesting to note that the τ_{CQ}-normalized halo current measurements in figure 6 exhibit similar rotation durations across machines. This is a preliminary indication that τ_{CQ} factors prominently into the scaling of the rotation duration, t_{rot}. Before addressing this scaling, however, the polarities and rotation directions in figure 6 warrant further investigation.

First, with regard to polarity, the two predominantly positive (red) halo current measurements in figure 6 (NSTX and AUG-C/DUAm) are acquired from halo current sensors on the outboard side of the divertor. Conversely, the three predominantly negative (blue) halo current measurements in figure 6 (C-Mod, AUG-W/DUIm, and DIII-D/R11) are acquired from sensors on the inboard side of the divertor. Upon examining the polarity of halo currents across the entire ITPA halo current rotation database, it becomes clear that, in addition to the inboard or outboard location of the sensors, the polarity of the toroidal field, B_T, controls the polarity of the halo currents. This conclusion is borne out in figure 7, which plots the signed maximum halo current measured by each sensor array, I_h, against the signed toroidal magnetic field, B_T. For the outboard sensor arrays in AUG, NSTX, and DIII-D, the halo current flows out of the wall for negative B_T and into the wall for positive B_T (figure 7(*a*)). For the inboard sensor arrays in C-Mod, AUG, and DIII-D, on the other hand, the halo current flows into the wall for negative B_T and out of the wall for positive B_T (figure 7(*b*)). These results, which are independent of the direction of the plasma current, indicate that the halo currents flow *paramagnetically* with respect to the toroidal field. The halo currents therefore act to conserve the toroidal flux in the disrupting plasma [11]. We note that the handful of NSTX and AUG data points that run counter to this trend represent a small number of disruptions ($\sim 1\%$) that contact the wall on the outboard (inboard) side of a nominally outboard (inboard) sensor array [8].

A second quantity of interest is the preferential direction of the halo current rotation. In figure 6, five of the eight sample halo current pulses rotate in the negative toroidal direction (clockwise). As shown in figure 8, it is the direction of the plasma current, I_p, that determines the preferential direction of the halo current rotation. In fact, all halo current pulses in the ITPA halo current rotation database that complete at least two full rotations ($|N_{rot}| > 2$) do so in the counter-I_p direction. Reversed-I_p data points from C-Mod confirm that the preferential direction of halo current rotation changes with a change in the direction of I_p. This result is obtained independent of the direction of B_T since reversed B_T data points are included for both C-Mod and DIII-D. While it is important to note that substantial co-I_p rotation is also frequently observed, any theory that seeks to explain halo current rotation must explain why the direction of rotation is preferentially counter-I_p.

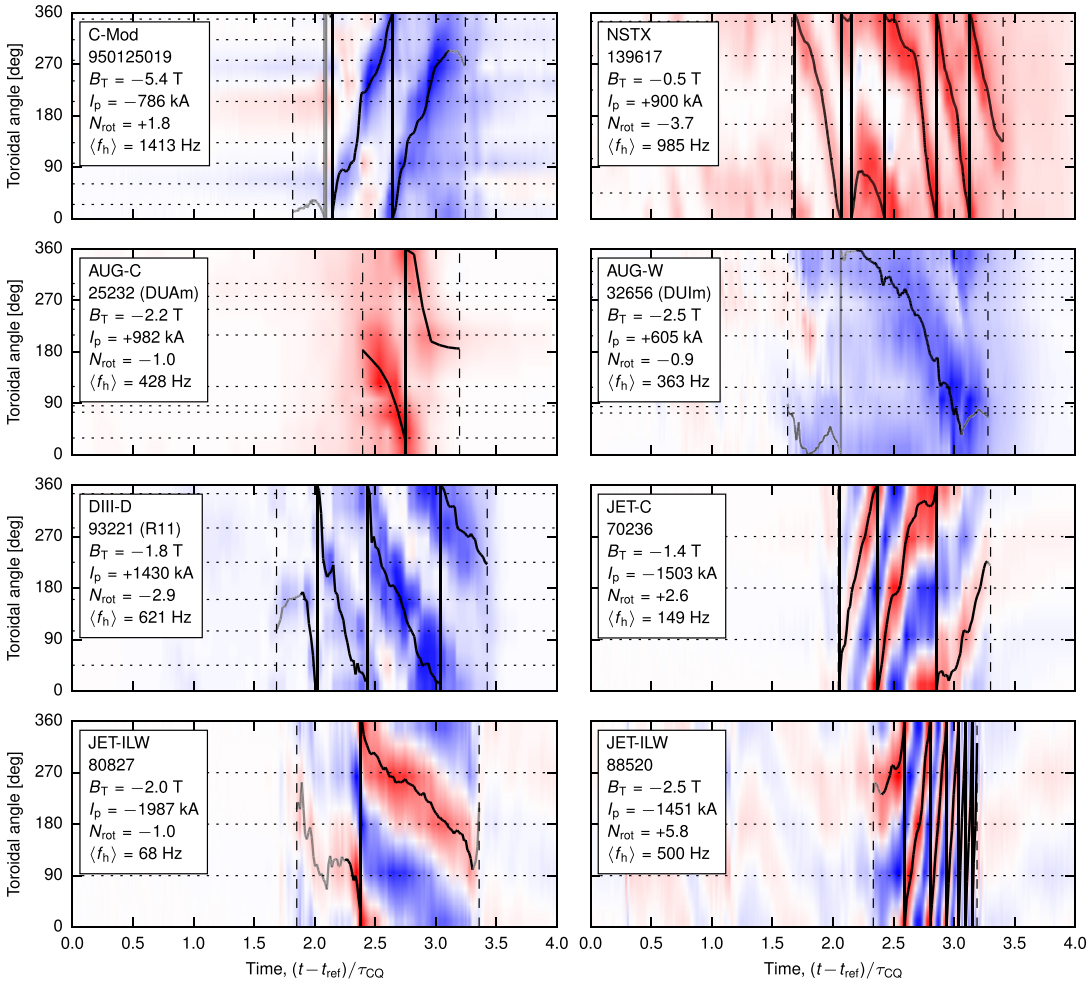

Figure 6. Rotating halo current examples sourced from across the ITPA halo current rotation database. The timebases are referenced to an arbitrary time point, t_{ref}, and normalized to the minimum current quench time, τ_{CQ}. In the C-Mod, NSTX, AUG, and DIII-D examples, the prevailing color of the halo currents indicates their polarity (red = positive = out of the wall; blue = negative = into the wall). In the JET examples, the I_p asymmetry measurements are symmetric about zero such that no polarity information is available. Several parameters of interest are listed for each discharge including the toroidal field, B_T, the plasma current, I_p, the total rotation count, N_{rot}, and the average rotation frequency, $\langle f_h \rangle$. The signed quantities (B_T, I_p, and N_{rot}) are referenced to right-handed toroidal coordinates. The vertical dashed lines delineate the asymmetry intervals over which the rotation is analyzed (see figures 5(*a*) and (*b*)). The details of the halo current polarity and the direction of rotation are discussed in the text.

5. Halo current rotation scalings

The current quench and halo current rotation analysis procedures in sections 3 and 4 provide the necessary data to develop empirical scalings for the halo current rotation duration and rotation frequency. In sections 5.1 and 5.2, we develop these empirical scalings by performing least squares regression on the t_{rot} and $\langle f_h \rangle$ data from the rotation analysis in section 4. Then, in section 5.3, the resulting scalings are used to project t_{rot}, $\langle f_h \rangle$, and N_{rot} to ITER.

5.1. The rotation duration scaling

The empirical t_{rot} scaling developed in this section uses the machine-specific minimum current quench time, τ_{CQ}, as the independent variable in the least squares regression. At first glance, it may seem surprising that τ_{CQ} rather than the shot-specific current quench time, t_{CQ}, is the best independent variable to choose. To qualitatively demonstrate why τ_{CQ} is the appropriate choice, figure 9 explores the relationship between t_{rot} and t_{CQ}. A quantitative comparison of the consequences of using t_{CQ} versus τ_{CQ} in the least squares regression of t_{rot} is included later in this section.

At this juncture, we down-select the ITPA halo current rotation database to include only halo current pulses that complete at least three-quarters of a rotation ($|N_{rot}| > 0.75$). This eliminates the locked or dithering cases that do not threaten to dynamically amplify the halo current forces. This down-selection cuts the database nearly in half, leaving 478 rotating discharges. Returning to figure 9, we see that, while there is a correlation between t_{rot} and t_{CQ} ($r_{corr} \simeq 0.84$), the longest current quenches in the database (toward the right) are strongly decorrelated from the measured rotation duration. The JET and NSTX databases, in particular, highlight the fact that t_{rot} spans a consistent range within each machine, regardless of the value of t_{CQ}. While the decorrelation between t_{CQ} and t_{rot} is not well understood, the fact that t_{rot} is more consistent from disruption to disruption than t_{CQ} hints that the conditions in

the halo region are somewhat decoupled from the conditions that govern the current quench.

Regardless of the physical mechanism that causes t_{rot} and t_{CQ} to decouple, the relative invariance of t_{rot} at high values of t_{CQ} suggests that t_{rot} is better correlated to the characteristic minimum current quench time, τ_{CQ}. This τ_{CQ} correlation is borne out in the empirical scaling of t_{rot} presented in figure 10. Here, least squares regression is used to determine the optimum logarithmic fit to the t_{rot} values in the ITPA halo current rotation database. The x-axis of figure 10 represents the least squares fit to t_{rot}, while the y-axis represents the t_{rot} measurements from the database. The least squares scaling function used here is

$$t_{rot} = C_t \left(\tau_{CQ}\right)^{\alpha_\tau}, \tag{7}$$

where τ_{CQ} is the sole independent variable and C_t and α_τ are the two regression parameters. The fitted values for these parameters are $C_t = 0.59 \pm 0.04$ and $\alpha_\tau = 0.92 \pm 0.01$ for τ_{CQ} and t_{rot} in units of seconds. Interestingly, the τ_{CQ} exponent is near unity, indicating that t_{rot} scales roughly in proportion to τ_{CQ}. The coefficient of determination for the t_{rot} scaling is $R^2_{fit} \simeq 0.82$, indicating a high quality fit in spite of the simple form of the scaling equation. The data in figure 10 are bracketed vertically by a logarithmic $3\sigma_t$ envelope, where $\sigma_t = 0.414$ is defined as the root mean-square error (RMSE) of the logarithmic fit. Note that all of the data points in the database fall within this $3\sigma_t$ envelope. Finally, and perhaps most importantly, the inclusion of additional independent variables (R, a, t_{CQ}, I_p, B_T) as factors in the regression equation does not meaningfully improve the quality of the fit (the R^2_{fit} value) in spite of the added degrees of freedom. As such, we conclude that the observed intra-machine variation must be caused either by hidden variables not available in the database or by random shot-to-shot variation. Finally, if t_{CQ} is used instead of τ_{CQ} as the independent regression variable, the resulting fit metrics of $R^2_{fit} = 0.71$ and $\sigma_t = 0.530$ are meaningfully degraded from the τ_{CQ} values. Thus, we conclude that τ_{CQ} is quantitatively the better regression variable.

The empirical t_{rot} scaling developed in figure 10 permits the projection of t_{rot} to ITER parameters. As indicated by x-axis extents of the yellow parallelogram in figure 10, the point-projected ITER t_{rot} values range from 30–96 ms, depending on the projected value of τ_{CQ} (see table 2). The vertical extents of the yellow parallelogram are set by the $3\sigma_t$ envelope that is determined from the RMSE of the least squares fit. The topmost corner of the ITER parallelogram suggests that t_{rot} values in ITER could exceed 300 ms if τ_{CQ} scales with $C(\eta^{-1}) = 4.2$ ms m^{-2}. If τ_{CQ} scales with $C(\eta^{-1}) = 1.2$ms m^{-2}, on the other hand, then the maximum t_{rot} are likely to be limited to ~100 ms. These projected values of t_{rot} will be used in section 5.3 to formulate a more comprehensive projection of halo current rotation in ITER.

Finally, since τ_{CQ} is a machine-specific quantity that has the same value for all of the data points from a given machine, each dataset in figure 10 is compressed into a vertical line. In order to investigate the distribution of t_{rot} values within these datasets, figure 11 plots the normalized rotation duration, t_{rot}/τ_{CQ}, sorted by machine. As expected from the least

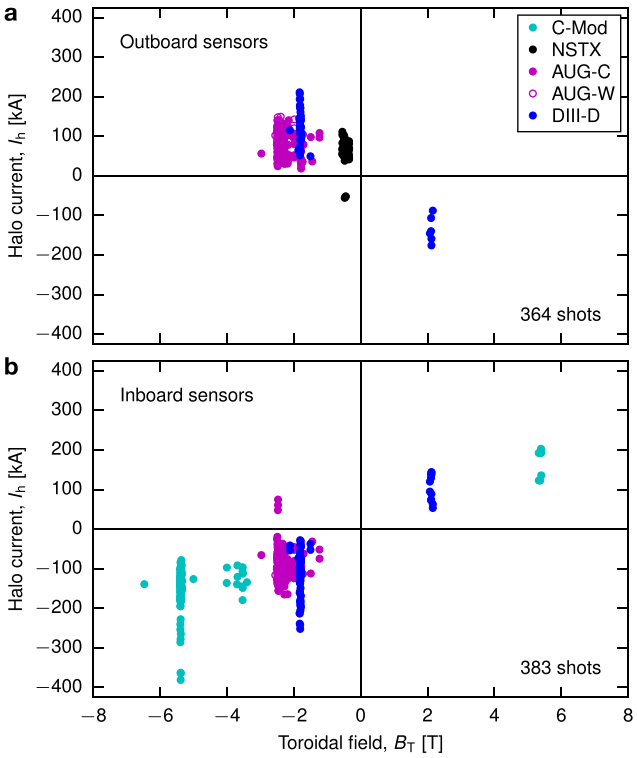

Figure 7. Halo current polarity with respect to the toroidal magnetic field, B_T. JET data are not included here since the I_p asymmetry measurements do not provide polarity information. (*a*) Sensors on the outboard divertor measure halo currents that flow out of the wall (positively) for negative B_T and into the wall (negatively) for positive B_T. (*b*) The results are reversed for sensors on the inboard divertor. These findings, which are independent of the direction of the plasma current, indicate that the poloidal direction of the halo currents is paramagnetic with respect to B_T.

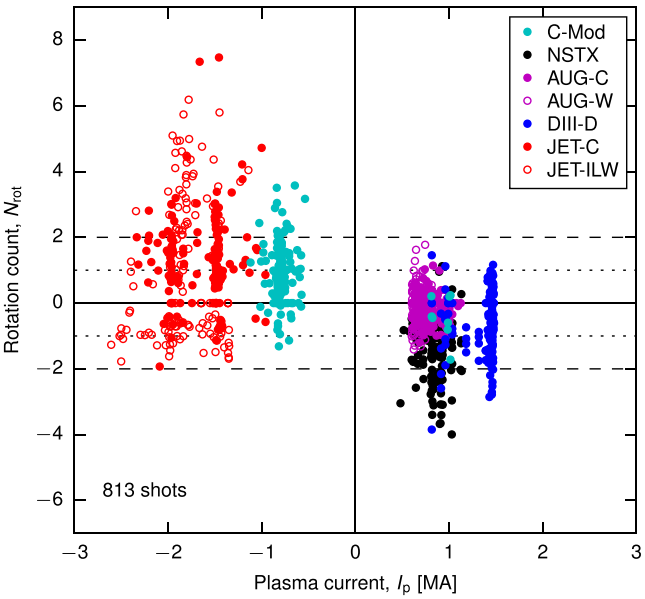

Figure 8. Halo current rotation with respect to the plasma current, I_p. All of the halo current pulses in the ITPA halo current rotation database that complete at least two full toroidal rotations ($|N_{rot}| > 2$) rotate against the direction of the plasma current (counter-I_p). Substantial co-I_p rotation is also possible These results are obtained independent of the direction of B_T.

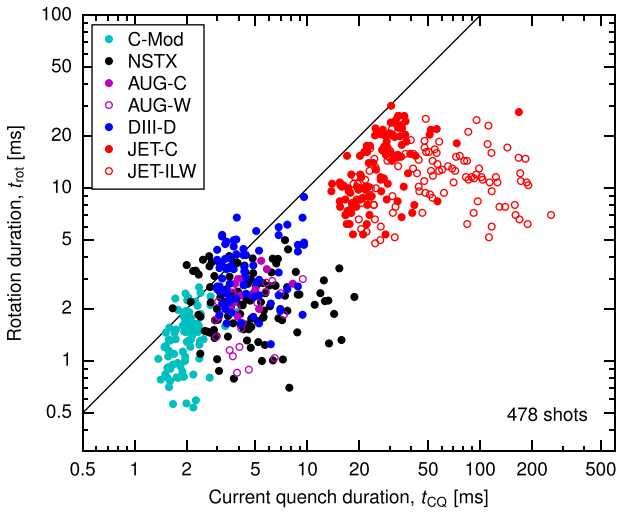

Figure 9. Halo current rotation duration, t_{rot}, versus the shot-specific current quench time, t_{CQ}. Only shots with $|N_{rot}| > 0.75$ are included. While it is clear that t_{CQ} and t_{rot} are correlated ($r_{corr} \simeq 0.84$), the longest current quench times do not produce correspondingly long rotation durations. This implies that t_{rot} is more likely to scale with the minimum current quench time, τ_{CQ}, than with the shot-specific quench time, t_{CQ}.

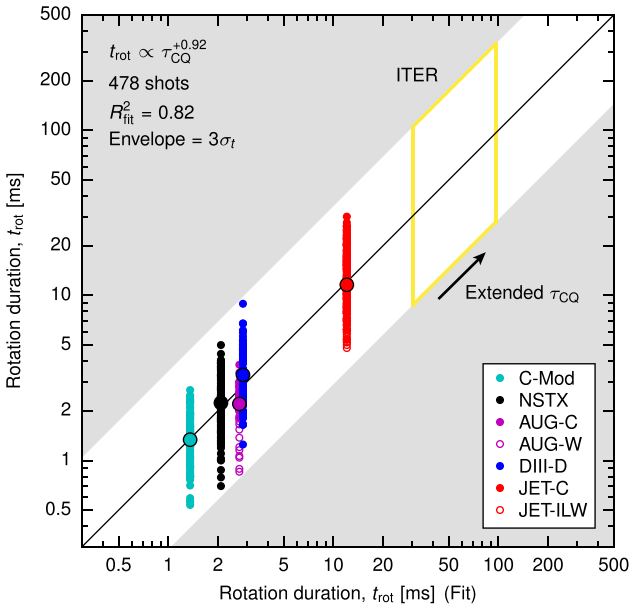

Figure 10. Empirical scaling of the halo current rotation duration, t_{rot}. The x-axis represents the fitted values of t_{rot}, while the y-axis represents the t_{rot} measurements from the database. Only shots with $|N_{rot}| > 0.75$ are included. The median of the dataset for each machine is plotted as a larger circle outlined in black. Least squares regression using equation (7) gives an empirical scaling of $t_{rot} \propto \tau_{CQ}^{+0.92}$ with a coefficient of determination of $R^2_{fit} \simeq 0.82$. The inclusion of other independent variables does not improve the fit. The t_{rot} data are bracketed in gray by a logarithmic $3\sigma_t$ envelope determined from the root mean-square error (RMSE) of the fit. This $3\sigma_t$ envelope is used to project t_{rot} to ITER parameters. The yellow parallelogram shows the results of this projection, which depends implicitly on the scaling of τ_{CQ}. See the text for further details.

squares fit, the majority of the measured t_{rot} values fall within a factor of two of τ_{CQ}. This is in spite of the fact that the shot-specific current quench time, t_{CQ}, can exceed τ_{CQ} by an order of magnitude (see figures 4 and 9). From the normalized t_{rot} distributions in figure 11, we conclude that the distribution of t_{rot} values is similar from machine to machine and furthermore that the bulk of the t_{rot} values are meaningfully longer than the minimum dwell time, $\tau_{min} = 0.3\ \tau_{CQ}$, that is used in the halo current rotation analysis procedure in section 4. This result validates the use of this τ_{min} value in the rotation analysis procedure.

5.2. The rotation frequency scaling

The remaining task is to develop an empirical scaling for the average halo current rotation frequency, $\langle f_h \rangle$. The scaling equation employed for $\langle f_h \rangle$ is given by

$$\langle f_h \rangle = C_f\, R^{\alpha_R} \left(t_{rot}/R\right)^{\alpha_t} \tag{8}$$

where the major radius, R, and the rotation duration, t_{rot}, are the independent variables, and C_f, α_R, and α_t are the regression parameters. The t_{rot}/R ratio is deliberately selected as a regression factor because, as will be shown in section 5.3, t_{rot}/R scales weakly when compared to the individual scalings of t_{rot} and R. This form of the scaling equation therefore emphasizes the key role of the major radius in setting the halo current rotation frequency.

Figure 12 shows the results of the $\langle f_h \rangle$ least squares regression. The fitted parameter values are $C_f = 25.4 \pm 4.2$, $\alpha_R = -1.10 \pm 0.03$, and $\alpha_t = -0.53 \pm 0.03$. The $\langle f_h \rangle$ values

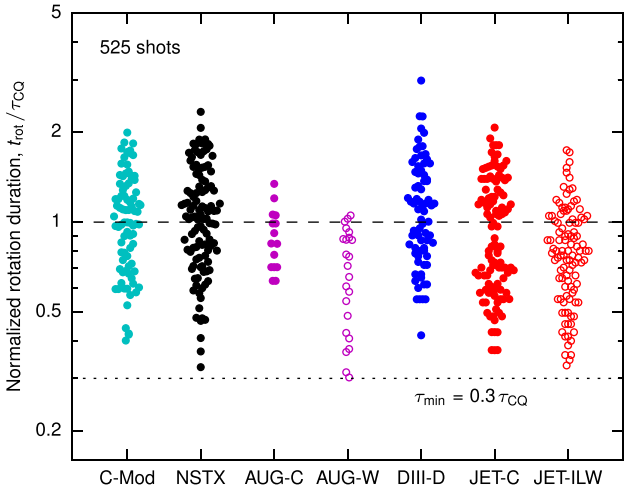

Figure 11. The halo current rotation duration, t_{rot}, normalized to the minimum current quench timescale, τ_{CQ}. The majority of measured t_{rot} values fall within a factor of two of τ_{CQ}. The dotted line represents the minimum dwell time, $\tau_{min} = 0.3\ \tau_{CQ}$, that is used in the halo current analysis procedure in section 4. The fact that the majority of the t_{rot} values are meaningful longer than τ_{min} validates its use in the analysis procedure.

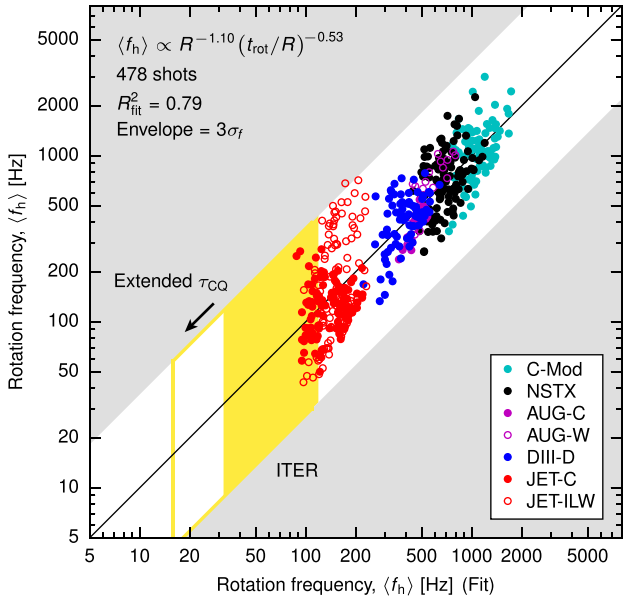

Figure 12. Empirical scaling of the average halo current rotation frequency, $\langle f_h \rangle$. Only shots with $|N_{rot}| > 0.75$ are included. Least squares regression using equation (8) gives an empirical scaling of $\langle f_h \rangle \propto R^{-1.10}(t_{rot}/R)^{-0.53}$ with a coefficient of determination of $R^2_{fit} \simeq 0.79$. Once again, the inclusion of other independent variables does not improve the fit. The $\langle f_h \rangle$ data are bracketed vertically by a $3\sigma_f$ envelope determined from the RMSE of the fit. The extrapolation to ITER (the yellow parallelogram) finds that halo current rotation is probable below the 20 Hz resonance threshold and that an extended τ_{CQ} projection (the unshaded region) leads to increasingly slow rotation. See the text for further details.

computed from these parameters are given units of hertz. The coefficient of determination for the $\langle f_h \rangle$ scaling is $R^2_{fit} \simeq 0.79$, indicating another good fit to the data. As with the t_{rot} scaling, a logarithmic $3\sigma_f$ envelope based on the RMSE of the fit ($\sigma_f = 0.431$) is used to bracket the $\langle f_h \rangle$ data. Finally, as before, the inclusion of additional independent variables (a, τ_{CQ}, t_{CQ}, I_p, B_T) as factors in the regression equation does not improve the fit. The intra-machine variation in $\langle f_h \rangle$ must therefore be attributed either to hidden variables not available in the database or to random shot-to-shot variation.

The empirical frequency scaling developed in figure 12 facilitates a projection of $\langle f_h \rangle$ to ITER parameters. The results of this projection are shown by the yellow parallelogram in figure 12. As with the projection in figure 10, the boundaries of the yellow parallelogram in figure 12 depend on the projection of τ_{CQ}. Here, τ_{CQ} propagates into the scaling through the t_{rot} term. The solid yellow parallelogram in figure 12 represents the projected frequency range if τ_{CQ} scales with $C(\eta^{-1}) = 1.2$ ms m^{-2}. The finite horizontal extent of the solid region results from the $3\sigma_t$ uncertainty envelope in the scaling of t_{rot}. If τ_{CQ} scales instead with $C(\eta^{-1}) = 4.2$ms m^{-2}, the projected range of frequencies extends down and to the left (into the unshaded region of the parallelogram). In either case, these projections indicate that some halo current rotation in ITER is likely to occur at frequencies below the 20 Hz resonance threshold. Since dynamic force amplification requires $N_{rot} \gtrsim 2$–3, however, the existence of resonant rotation at frequencies below

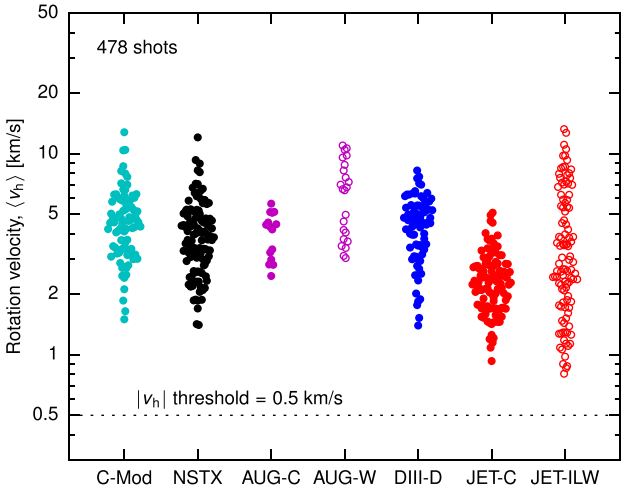

Figure 13. Average halo current rotation velocity, $\langle v_h \rangle$, sorted by machine. As indicated by the empirical $\langle f_h \rangle$ scaling developed in figure 12, the distribution of velocities is surprisingly consistent from machine to machine. All velocities in the database fall within a 0.7–17 km s^{-1} envelope. Slightly elevated velocities are measured in both the AUG-W and JET-ILW metal-wall datasets when compared to their carbon counterparts. The dotted line shows the $|v_h| = 0.5$ km s^{-1} velocity threshold used in the rotation analysis in section 4. This threshold is well below any measured rotation velocities in the database.

20 Hz does not necessarily imply that dynamic amplification will occur. A full assessment of the projection to ITER is carried out in section 5.3.

The most notable feature of the empirical frequency scaling developed in figure 12 is that the frequency scales roughly with the inverse major radius ($\alpha_R \sim -1.1$). As such, the average rotation velocity, $\langle v_h \rangle \equiv 2\pi R \langle f_h \rangle$, scales as $\langle v_h \rangle \sim R^{-0.1}(t_{rot}/R)^{-0.5}$. As previously mentioned, t_{rot}/R varies weakly when compared to other parameters. It is therefore reasonable to expect $\langle v_h \rangle$ to change only weakly from machine to machine. To demonstrate this effect, figure 13 plots $\langle v_h \rangle$ across the ITPA halo current rotation database, sorted by machine. This figure shows that, like the normalized rotation durations in figure 11, the distribution of velocities across the database is quite consistent. Interestingly, both the AUG-W and JET-ILW metal-wall datasets include faster rotation velocities than their carbon counterparts (AUG-C and JET-C, respectively). That being said, the JET-ILW dataset includes both the fastest and slowest velocities in the entire database, indicating that metal walls do not necessarily eliminate the lower velocity points in the distribution. A key takeaway from these data is that any theory that seeks to explain halo current rotation must explain the relative consistency of the rotation velocity from machine to machine.

We note here that the consistent halo current rotation velocity is both surprising and somewhat difficult to explain. One of the few halo region parameters that is expected to be independent of the magnetic field and other key machine parameters is the sound speed, c_s, since it only depends on the halo temperature. We postulate that the halo temperature is likely to be relatively consistent from disruption to disruption because it is moderated by the high parallel thermal

Table 3. Summary of least squares regression parameters for the empirical halo current rotation scalings derived from the ITPA halo current rotation database. For these scalings, τ_{CQ} and t_{rot} must be in units of seconds, R in units of meters, and $\langle f_h \rangle$ in units of hertz. The logarithmic root mean-square error (RMSE) values for each fit, σ_t and σ_f, are also listed here. For a given point-projected quantity x with an RMSE of σ, the 3σ range of expected values is given by $x \cdot e^{\pm 3\sigma}$.

Scaling equation	Regression parameter	
$t_{rot} = C_t \left(\tau_{CQ}\right)^{\alpha_\tau}$	C_t	0.59 ± 0.04
	α_τ	0.92 ± 0.01
$\langle f_h \rangle = C_f R^{\alpha_R} \left(t_{rot}/R\right)^{\alpha_t}$	C_f	25.4 ± 4.2
	α_R	-1.10 ± 0.03
	α_t	-0.53 ± 0.03
Root mean-square error	σ_t	0.414
	σ_f	0.431

conductivity between the halo plasma and the wall. Thus, if the halo current rotation is sonically driven, then a consistent halo plasma temperature could explain the relative parameter independence of $\langle v_h \rangle$. See section 6 for more discussion.

One final result (not shown here) is that neither the normalized rotation duration, t_{rot}/τ_{CQ}, nor the rotation velocity, $\langle v_h \rangle$, correlate with the amplitude of the halo current asymmetry. The asymmetry amplitude can be quantified by averaging the $n = 1$ fit parameter, h_1, over the main rotation interval (see section 4). This analysis indicates that both t_{rot}/τ_{CQ} and $\langle v_h \rangle$ are virtually uncorrelated with the average asymmetry amplitude ($|r_{corr}| < 0.25$). As such, large-amplitude events are equally likely to occur at any of the observed rotation durations and rotation velocities.

5.3. Projection to ITER

In sections 5.1 and 5.2, empirical scalings for the halo current rotation duration, t_{rot}, and rotation frequency, $\langle f_h \rangle$, are derived from the ITPA halo current rotation database. The resulting scalings for t_{rot} and $\langle f_h \rangle$ are summarized in table 3. As a final step, we now use these scalings to develop a projection of the overall behavior of rotating halo currents in ITER.

First, the empirical scalings in table 3 can be combined to give the following approximate scalings for the rotation velocity, $\langle v_h \rangle$, and the total number of rotations, N_{rot}, in terms of the quantity τ_{CQ}/R:

$$\begin{aligned} t_{rot} &\propto \left(\tau_{CQ}\right)^{+0.9} \\ \langle f_h \rangle &\propto R^{-1.1} \left(t_{rot}/R\right)^{-0.5} \\ \langle v_h \rangle &= 2\pi R \cdot \langle f_h \rangle \sim \left(\tau_{CQ}/R\right)^{-0.5} \\ N_{rot} &= t_{rot} \cdot \langle f_h \rangle \sim R^{-0.1} \left(\tau_{CQ}/R\right)^{+0.4} \end{aligned} \tag{9}$$

The quantity τ_{CQ}/R increases weakly with machine size. As such, we expect $\langle v_h \rangle$ and N_{rot} to change only modestly from machine to machine. Table 4 lists the values of τ_{CQ}/R along with point projections of $\langle v_h \rangle$ and N_{rot} for each machine. Given the conclusions of figure 13 regarding the consistent range of $\langle v_h \rangle$, the very modest decrease in $\langle v_h \rangle$ with increasing machine size comes as no surprise. Equation (9) and table 4 also indicate that N_{rot} increases only slightly with increasing machine size. Thus, while t_{rot} increases by orders of magnitude and $\langle f_h \rangle$ decreases by orders of magnitude, their product, N_{rot}, grows by less than a factor of three from present-day machines to ITER.

Table 4. Values of the quantity τ_{CQ}/R for each machine and the resulting point projections of the the rotation velocity, $\langle v_h \rangle$, and the total number of rotations, N_{rot}. The latter two quantities scale with τ_{CQ}/R according to equation (9).

Machine	τ_{CQ}/R (ms m^{-1})	$\langle v_h \rangle$ (km s^{-1})	N_{rot}
C-Mod	2.0	4.4	1.4
NSTX	2.5	3.9	1.5
AUG	1.7	4.5	1.2
DIII-D	1.8	4.4	1.2
JET	4.9	2.6	1.7
ITER (min τ_{CQ})	6.4	2.2	1.7
ITER (max τ_{CQ})	22	1.2	3.0

To complete the projection to ITER, the empirical scalings listed in table 3 are combined in figure 14 with the t_{rot} and N_{rot} data from the ITPA halo current rotation database. Here, each panel presents the N_{rot} versus t_{rot} parameter space for one of the machines in the database. The shaded parallelograms represent the projected range of t_{rot} and N_{rot} for each machine according to the empirical scalings in table 3. The overplotted data points, on the other hand, represent the measurements of t_{rot} and N_{rot} extracted from the database. In each panel, a dashed line at $N_{rot} = 2$ and a solid line at $N_{rot} = 3$ delineate the thresholds for dynamic force amplification. Finally, since the rotation frequency is given by $\langle f_h \rangle = N_{rot}/t_{rot}$, bands of constant frequency appear as diagonal lines. Three such lines with values of $\langle f_h \rangle = 3$, 8, and 20 Hz are shown on the right hand side of each panel. These particular frequency values are selected for their relationship to the resonance zones in ITER.

Figure 14 shows that virtually all of the data points in the database fall within the projected parallelograms for their respective machines. One notable feature of figure 14 is that the AUG data points do not populate as much of their projected parallelogram as do the other machines. More specifically, AUG favors shorter rotation durations and correspondingly lower rotation counts. We hypothesize that this trend is due to the fact that all of the AUG disruptions in the database are downward-moving VDEs that disrupt into the lower divertor. These downward-moving VDEs are selected based on the location of the toroidally resolved DUIm and DUAm shunt tile arrays. It may be the case, however, that upward-moving VDEs in AUG produce longer halo current rotation durations. In JET, which has a similar lower divertor structure to AUG, upward-moving VDEs have long been known to produce larger forces than their downward-moving counterparts [23–25, 37]. It is believed that the lower divertor structure short-circuits the halo current path in the wall during downward-moving VDEs, thereby limiting the halo current duration. We therefore hypothesize that a similar up/down asymmetry may be the cause of the short rotation durations in the AUG dataset. If the divertor geometries of AUG and JET are responsible for reducing the impact of halo currents in downward-moving

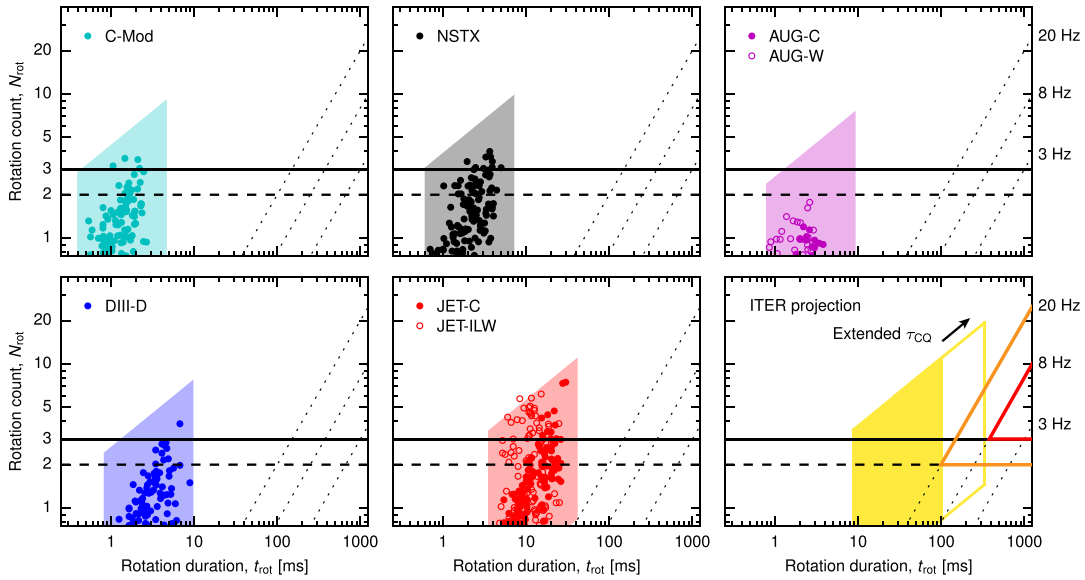

Figure 14. Parameter space of the total number of rotations, N_{rot}, versus the rotation duration, t_{rot}, sorted by machine. The shaded parallelograms represent the projected range of halo current rotation for a given machine based on the empirical scalings in table 3. The data points, on the other hand, represent the measurements of t_{rot} and N_{rot} in the database. Each panel contains a dashed line at $N_{rot} = 2$ and a solid line at $N_{rot} = 3$ to delineate the dynamic amplification thresholds. The three dotted diagonal lines are lines of constant frequency at $\langle f_h \rangle = 3$, 8, and 20 Hz. For the ITER projection at the bottom right, the solid parallelogram represents the projected rotation range if the minimum current quench time, τ_{CQ}, scales with $C(\eta^{-1}) = 1.2$ ms m^{-2} (see section 3). The unshaded extension to the parallelogram represents the projected range if the τ_{CQ} value scales instead with $C(\eta^{-1}) = 4.2$ ms m^{-2}. This latter region projects that substantial halo current rotation could occur in the ITER resonance zones (outlined in orange and red). As such, the prospect of damaging halo current rotation during unmitigated disruptions in ITER cannot be ruled out.

VDEs, then we must also conclude that the various lower divertor geometries of C-Mod (1995–1996), DIII-D (1997), and NSTX do not have a similar short-circuiting effect on the halo currents. Further study of the halo current paths in each device, using either experimental or numerical tools [45, 46], would be required to verify this assertion.

A second notable feature of figure 14 is that the JET parallelogram appears to be more populated than that of the other machines. This is largely due to the inclusion of the JET-ILW data. If only the JET-C data are considered, the JET database looks much like those of C-Mod, NSTX, and DIII-D where the upper region of the parallelogram is largely unpopulated. When the JET-ILW data are included, however, the faster observed rotation velocities in JET-ILW (see figure 13) produce higher-frequency rotation that populates the upper regions of the JET parallelogram. Given the deliberate similarities between the wall material in the JET-ILW and ITER cases, it is reasonable to expect that ITER might have a similar distribution of halo current rotation to that of JET-ILW.

The final step is to evaluate the overall projection to ITER. As stated in section 1, the key question for halo current rotation in ITER is whether the halo currents are likely to complete 2–3 full rotations at frequencies below 20 Hz. With this criterion in mind, the lower right-hand panel of figure 14 shows the projected range of ITER halo current rotation. The solid yellow parallelogram represents the projected range if the minimum current quench time, τ_{CQ}, scales with $C(\eta^{-1}) = 1.2$ ms m^{-2} (see section 3). With this projection, we see that substantial rotation ($|N_{rot}| \lesssim 10$) is to be expected at frequencies above $\langle f_h \rangle = 20$ Hz. However, because the rotation duration is limited to $t_{rot} \lesssim 100$ ms in this case, the lowest rotation frequency that achieves three complete rotations is $\langle f_h \rangle \simeq 30$ Hz. As such, if $C(\eta^{-1}) = 1.2$ ms m^{-2} provides an accurate projection for τ_{CQ}, then ITER is likely to avoid damaging halo current rotation in the $\langle f_h \rangle < 20$ Hz resonance zones.

As with the t_{rot} and $\langle f_h \rangle$ projections in figures 10 and 12, however, we must consider the case where τ_{CQ} proves to be longer than expected in ITER. To this end, the unshaded region of the ITER parallelogram in figure 14 shows the projected halo current rotation if τ_{CQ} scales with $C(\eta^{-1}) = 4.2$ ms m^{-2}. This extended-τ_{CQ} projection gives a maximum rotation duration of $t_{rot} \simeq 330$ ms, which would produce $N_{rot} = 3$ at $\langle f_h \rangle \gtrsim 9$ Hz and $N_{rot} = 2$ at $\langle f_h \rangle \gtrsim 6$ Hz. Such halo current rotation parameters could produce damaging dynamic force amplification in ITER. Thus, given the extended-τ_{CQ} projection for N_{rot} and $\langle f_h \rangle$ and the latent uncertainties in the scaling of τ_{CQ}, the prospect of damaging halo current rotation during unmitigated disruptions in ITER cannot be ruled out.

One final consideration is what would happen if the VDE growth time of $\tau_{vert} \sim 500$ ms rather than the $\mathcal{L}/\mathcal{R}$ inductive quench time of $\tau_{ind} \lesssim 130$ ms governs the halo current rotation duration, t_{rot}, in ITER. The resulting extended rotation durations would push the ITER projection in figure 14 further up and to the right and directly into the heart of the mechanical resonance zones. Unfortunately, as described in section 3, the five machines in the ITPA halo current rotation database each have VDE growth times on the order of a few milliseconds. This prevents a data-driven identification of the role of τ_{vert} in setting t_{rot}. That being said, the possibility that

the extended VDE growth time in ITER could generate long halo current rotation durations of 500 ms or more is further cause for concern that ITER may be susceptible to damage from halo current rotation during unmitigated disruptions.

6. Summary and discussion

This paper presents an ITPA-initiated multi-machine analysis of halo current rotation. Seven datasets spanning five different machines are combined to develop empirical scalings for the halo current rotation duration, t_{rot}, and the rotation frequency, $\langle f_h \rangle$. These scalings, which rely only on the machine-specific minimum current quench time, τ_{CQ}, and the major radius, R, are used to project the behavior of rotating halo currents in ITER. The key findings are that substantial halo current rotation is to be expected above $\langle f_h \rangle = 20$ Hz, and that, if the τ_{CQ} value in ITER proves to be at the upper end of the projected range, potentially damaging resonant rotation with $N_{rot} \gtrsim 2$–3 in the frequency range of $\langle f_h \rangle = 6$–20 Hz could occur during unmitigated disruptions.

In addition to the halo current rotation scaling, the results reported in this paper identify several phenomena that must be explained by any theory of halo current rotation. First, the preferential direction of halo current rotation is counter-I_p, independent of B_T and other parameters. It is important to note, however, that substantial co-I_p rotation can occur and that the direction of rotation can reverse within a single disruption. Additionally the halo current rotation velocity, $\langle v_h \rangle$, changes very little from machine to machine. This rotation velocity appears to be insensitive to most machine parameters, including I_p and B_T. Thus, as previously conjectured by Zakharov *et al* [47], the mechanism that drives halo current rotation is likely to be independent of the core plasma parameters. Several results presented in this paper indicate that the conditions in the halo region are decoupled from the conditions in the core. First, in section 3, the rotation duration, t_{rot}, is found to be more consistent from disruption to disruption than the current quench time, t_{CQ}. Additionally, the consistent halo current rotation velocity indicates that similar halo region conditions are achieved over a wide variety of machine parameters.

As described in section 5.2, we postulate that the halo current rotation may be sonically driven. This is because the sound speed, c_s, is one of the few halo region parameters that is expected to be independent of I_p and B_T. It instead depends only on the halo plasma temperature, which is likely to be moderated by the high parallel thermal conductivity between the halo plasma and the sheath at the wall. For a halo plasma temperature of $T_{e,halo} \sim 5$ eV, the sound speed will be $c_s \sim 30$ km s^{-1} such that the observed halo current rotation velocities of $\langle v_h \rangle = 0.7$–17 km s^{-1} correspond to rotation speeds of up to $0.5\,c_s$. If the rotation is in fact sonically driven, then the range of observed rotation velocities will correspond to the typical range of halo temperatures produced in each device. This range of temperatures is likely indicative of differences in the halo region density and in the amount of ohmic power deposited by the halo currents [44].

The possible relationship between the halo plasma sound speed and halo current rotation has already been suggested by Boozer [39], though the rotation mechanisms described therein are not independent of the toroidal magnetic field, B_T. Additionally, experimental evidence from laboratory magnetic flux rope experiments indicates that sonic flows can cause a magnetohydrodynamic kink mode to rotate [48–51]. The magnetic flux ropes in these experiments resemble the current-carrying helical flux tubes in the halo plasma in that both configurations constitute low-density, magnetized arc discharges. As such, exploring the similarities and differences between these two systems may provide further insight into the origin of halo current rotation.

Acknowledgments

This material is based upon work supported by the U.S. Department of Energy, Office of Science, Office of Fusion Energy Sciences, has been authored by Princeton University under Contract Number DE-AC02-09CH11466 with the U.S. Department of Energy and using the following DOE Office of Science user facilities: the DIII-D National Fusion Facility (award DE-FC02-04ER54698), and Alcator C-Mod (award DE-FG02-94ER54232). This work has also been carried out within the framework of the EUROfusion Consortium and has received funding from the Euratom research and training programme 2014–2018 under grant agreement No 633053 and from the RCUK Energy Programme [grant number EP/I501045]. The views and opinions expressed herein do not necessarily reflect those of the European Commission.

The authors thank the many physicists, engineers, and technicians who designed, built, and operated the halo current sensors that have contributed data to the ITPA halo current rotation database. These include L. Giannone of IPP Garching and M. Schaffer, T. Evans, and E.J. Strait of General Atomics. CEM thanks D. Pfefferlé, M.D. Boyer, J.W. Berkery, R.J. Buttery and W.M. Solomon for valuable input. The NSTX, DIII-D, and C-Mod data shown this paper can be obtained in digital format at http://arks.princeton.edu/ark:/88435/dsp01sn00b1428.

ORCID iDs

C.E. Myers https://orcid.org/0000-0003-4539-8406

References

[1] Strait E.J., Lao L.L., Luxon J.L. and Reis E.E. 1991 *Nucl. Fusion* **31** 527
[2] Andrew P., Miele P., Noll P., Pearce R., Pick M. and Rossi L. 1995 Measured currents in JET limiters during disruptions *Proc. 16th IEEE/NPSS Symp. on Fusion Engineering (Champaign, IL, USA, October 1995)* vol 1 pp 770–3
[3] Granetz R.S., Hutchinson I.H., Sorci J., Irby J.H., LaBombard B. and Gwinn D. 1996 *Nucl. Fusion* **36** 545
[4] Neyatani Y., Yoshino R., Nakamura Y. and Sakurai S. 1999 *Nucl. Fusion* **39** 559
[5] Knight P., Castle G., Morris A., Caloutsis A. and Gimblett C. 2000 *Nucl. Fusion* **40** 325

[6] Counsell G.F., Martin R., Pinfold T., Taylor D. and The MAST Team 2007 *Plasma Phys. Control. Fusion* **49** 435
[7] Pautasso G., Giannone L., Gruber O., Herrmann A., Maraschek M., Schuhbeck K.H. and The ASDEX Upgrade Team 2011 *Nucl. Fusion* **51** 043010
[8] Gerhardt S.P, Menard J., Sabbagh S. and Scotti F. 2012 *Nucl. Fusion* **52** 063005
[9] Roccella R., Roccella M., Riccardo V., Chiocchio S. and JET Contributors 2016 *Nucl. Fusion* **56** 106010
[10] Pomphrey N., Bialek J. and Park W. 1998 *Nucl. Fusion* **38** 449
[11] Humphreys D.A. and Kellman A.G. 1999 *Phys. Plasmas* **6** 2742–56
[12] Pick M.A., Noll P., Barabaschi P., Marcus F.B. and Rossi L. 1991 Evidence of halo currents in JET *Proc. 14th IEEE/NPSS Symp. on Fusion Engineering (San Diego, CA, USA, 30 October–3 September 1991)* vol 1 pp 187–90
[13] Riccardo V., Andrew P., Kaye A. and Noll P. 2002 Disruption design criteria for JET in-vessel components *Proc. 19th IEEE/NPSS Symp. on Fusion Engineering (Atlantic City, NJ, USA, 20–5 January 2002)* pp 384–7
[14] Wesley J.C. *et al* 2006 Disruption characterization and database activities for ITER *21st IAEA Fusion Energy Conf. (Chengdu, China, 16–21 October 2006) p* IT/P1–21 (www-naweb.iaea.org/napc/physics/FEC/FEC2006/papers/it_p1-21.pdf)
[15] Sugihara M., Shimada M., Fujieda H., Gribov Y., Ioki K., Kawano Y., Khayrutdinov R., Lukash V. and Ohmori J. 2007 *Nucl. Fusion* **47** 337
[16] Hender T.C., *et al*, The ITPA MHD, Disruption and Magnetic Control Topical Group 2007 *Nucl. Fusion* **47** S128
[17] Wesley J.C. *et al* 2010 Disruption, halo current and rapid shutdown database activities for ITER *23rd IAEA Fusion Energy Conf. (Daejeon, South Korea, 11–6 October 2010) p* ITR/P1–26 (www-naweb.iaea.org/napc/physics/FEC/FEC2010/papers/itr_p1-26.pdf)
[18] Schioler T., Bachmann C., Mazzone G. and Sannazzaro G. 2011 *Fusion Eng. Des.* **86** 1963–6
[19] Bachmann C. *et al* 2011 *Fusion Eng. Des.* **86** 1915–9
[20] Lehnen M. *et al* 2015 *J. Nucl. Mater.* **463** 39–48
[21] Schaffer M. and Leikind B. 1991 *Nucl. Fusion* **31** 1750
[22] Gerhardt S.P., Fredrickson E., Guttadora L., Kaita R., Kugel H., Menard J. and Takahashi H. 2011 *Rev. Sci. Instr.* **82** 103502
[23] Noll P., Andrew P., Buzio M., Litunovsky R., Raimondi T., Riccardo V. and Verrecchia M. 1997 Present understanding of electromagnetic behaviour during disruptions in JET *Proc. 19th Symp. on Fusion Technology (Lisbon, Portugal, 16–20 September 1996)* pp 751–4
[24] Andrew P., Noll P. and Riccardo V. 1998 The relation between halo currents and plasma displacement/deformation in JET *Proc. 17th IEEE/NPSS Symp. on Fusion Engineering (San Diego, CA, USA, 6–10 October 1997)* pp 108–11
[25] Riccardo V., Noll P. and Walker S. 2000 *Nucl. Fusion* **40** 1805
[26] Riccardo V., Hender T.C., Lomas P.J., Alper B., Bolzonella T., de Vries P., Maddison G.P. and The JET-EFDA Contributors 2004 *Plasma Phys. Control. Fusion* **46** 925
[27] Fitzpatrick R. 2007 *Phys. Plasmas* **14** 062505
[28] Zakharov L.E. 2008 *Phys. Plasmas* **15** 062507
[29] Strauss H.R., Paccagnella R. and Breslau J. 2010 *Phys. Plasmas* **17** 082505
[30] Fitzpatrick R. 2011 *Nucl. Fusion* **51** 053007
[31] Breslau J.A. and Bhattacharjee A. 2015 *Phys. Plasmas* **22** 062506
[32] Manickam J., Boozer A. and Gerhardt S. 2012 *Phys. Plasmas* **19** 082103
[33] Lehnen M., *et al* and JET EFDA Contributors 2013 *Nucl. Fusion* **53** 093007
[34] Gerasimov S., *et al* and Contributors J 2015 *Nucl. Fusion* **55** 113006
[35] Evans T.E., Kellman A.G., Humphreys D.A., Schaffer M.J., Taylor P.L., Whyte D.G., Jernigan T.C., Hyatt A.W. and Lee R.L. 1997 *J. Nucl. Mater.* **241–3** 606–11
[36] Gerhardt S.P. 2013 *Nucl. Fusion* **53** 023005
[37] Gerasimov S.N., Hender T.C., Morris J., Riccardo V., Zakharov L.E. and JET-EFDA Contributors 2014 *Nucl. Fusion* **54** 073009
[38] Boozer A.H. 2012 *Phys. Plasmas* **19** 052508
[39] Boozer A.H. 2015 *Phys. Plasmas* **22** 102511
[40] Strauss H. 2015 *Phys. Plasmas* **22** 082509
[41] Riccardo V., *et al* and JET-EFDA Contributors 2010 *Plasma Phys. Control. Fusion* **52** 124018
[42] de Vries P.C., *et al* and JET EFDA Contributors 2012 *Plasma Phys. Control. Fusion* **54** 124032
[43] Eidietis N., Gerhardt S., Granetz R., Kawano Y., Lehnen M., Lister J., Pautasso G., Riccardo V., Tanna R., Thornton A. and The ITPA Disruption Database Participants 2015 *Nucl. Fusion* **55** 063030
[44] Kiramov D.I., Lehnen M., Khayrutdinov R. and Lukash V. 2016 ITER disruption simulations with improved power balance in the halo region *Proc. 43rd EPS Conf. Plasma Physics (Leuven, Belgium, July 2016)* p P4.071 (http://ocs.ciemat.es/EPS2016PAP/pdf/P4.071.pdf)
[45] Bettini P. and Specogna R. 2014 *J. Comput. Phys.* **273** 100–17
[46] Albanese R., Carpentieri B., Cavinato M., Minucci S., Palmaccio R., Portone A., Rubinacci G., Testoni P., Ventre S. and Villone F. 2015 *Fusion Eng. Des.* **94** 7–21
[47] Zakharov L.E., Galkin S.A., Gerasimov S.N. and JET-EFDA Contributors 2012 *Phys. Plasmas* **19** 055703
[48] Furno I., Intrator T.P., Ryutov D.D., Abbate S., Madziwa-Nussinov T., Light A., Dorf L. and Lapenta G. 2006 *Phys. Rev. Lett.* **97** 015002
[49] Bergerson W.F., Forest C.B., Fiksel G., Hannum D.A., Kendrick R., Sarff J.S. and Stambler S. 2006 *Phys. Rev. Lett.* **96** 015004
[50] Ryutov D.D., Furno I., Intrator T.P., Abbate S. and Madziwa-Nussinov T. 2006 *Phys. Plasmas* **13** 032105
[51] Oz E., Myers C.E., Yamada M., Ji H., Kulsrud R.M. and Xie J. 2011 *Phys. Plasmas* **18** 102107
[52] Litaudon X. *et al* 2017 *Nucl. Fusion* **57** 102001